Research Article

New Structured Illumination Technique for the Inspection of High-Reflective Surfaces: Application for the Detection of Structural Defects without any Calibration Procedures

Yannick Caulier,[1] Klaus Spinnler,[1] Salah Bourennane,[2] and Thomas Wittenberg[1]

[1] *Fraunhofer-Institut für Integrierte Schaltungen IIS, Am Wolfsmantel 33, 91058 Erlangen, Germany*
[2] *GSM, Institut Fresnel, CNRS-UMR 6133, École Centrale Marseille, Université Aix-Marseille III, D.U. de Saint-Jérôme,
  Marseille Cedex 20, France*

Correspondence should be addressed to Yannick Caulier, cau@iis.fraunhofer.de

We present a novel solution for automatic surface inspection of metallic tubes by applying a structured illumination. The strength of the proposed approach is that both structural and textural surface defects can be visually enhanced, detected, and well separated from acceptable surfaces. We propose a machine vision approach and we demonstrate that this technique is applicable in an industrial setting. We show that recording artefacts drastically increases the complexity of the inspection task. The algorithm implemented in the industrial application and which permits the segmentation and classification of surface defects is briefly described. The suggested method uses "perturbations from the stripe illumination" to detect, segment, and classify any defects. We emphasize the robustness of the algorithm against recording artefacts. Furthermore, this method is applied in 24 h/7 day real-time industrial surface inspection system.

1. INTRODUCTION

One essential part of nondestructive surface inspection techniques working in the visible light domain is the choice of the appropriate illumination. Such an illumination allows to increase the visibility of defective surfaces without amplifying nondefective surface regions. In general, revealing more than one type of defect necessitates at least two complementary illumination technologies. As far as structural or textural defective surfaces have to be inspected, a *directed* illumination to enhance the visibility of *structural* defects or a *diffuse* illumination to reveal *textural* defects [1] is required. Hence, the primary goal of this work is to propose a new structured illumination technology that reveals both the two types of defective parts on *specular* surfaces.

In general, the application of *structured illumination* techniques serves two major purposes: the first deals with the retrieval of the *depth information* of a scene yielding an exact three-dimensional reconstruction. The second deals with *recovering the shape* of an observed object. The most common way is the projection of certain pattern of a structured light in such a way that the knowledge of the projected pattern combined with the observed deformation of the structure on the object surface permits the retrieval of accurate depth information of the scene [2]. This method can be improved by using more complex patterns, such as *encoded light* [3], *color-coded light* [4], or *Moire projection* [5]. The principle of all these methods is the combination of three-dimensional information obtained by one or more of calibrated cameras with information depicted in disturbances of the projected light pattern. In contrast to these solutions, Winkelbach and Wahl [6] proposed a reconstruction method of shapes in the scene with only one stripe pattern and one camera by computing the normal surface.

In opposite, a *diffuse illumination* technique is used when object surfaces have to be inspected with respect to their texture. The aim of this illumination is to reveal different surface types differing from their roughness and/or their color. The former influences the image brightness of the depicted surfaces whereas the latter affects the type and the intensity of the color. The choice of using grey (e.g., automatic inspection of paper [7] or metallic surfaces [8]) or color (e.g., integrity

inspection of food articles [9] or wood surface inspection images depends on the application task.

In an industrial inspection and quality assurance workflows, the main task of a human inspector is to visually classify object surfaces as nondefective or as defective. Since such visual inspection tasks are tedious and time consuming, machine vision systems are more and more applied for automatic inspection. The two major constraints imposed by an industrial inspection process are the high quality and the high throughput of the objects to analyze.

The choice of an illumination technique is strongly motivated by the inspection task. An appropriate lighting is all the more important as it represents the first element of a machine vision workflow. The inspection systems of metallic surfaces for industrial purpose involve manifold illumination techniques. We found two different quantitative approaches to reveal both textural and structural defects on metallic surfaces. In this context, quantitative means that the defective surfaces are detected and not measured, as it is the case for qualitative applications.

The first use retroreflective screens [10] as initially proposed by Marguerre [11] to reveal deflections of reflective surfaces. This technique has the advantage to reveal both kinds of defective surfaces (textural and structural) but with one inconvenient that both have similar appearances in the images so that they cannot be discriminated afterwards.

The second necessitates at least two different illumination techniques. The Parsytec company [12] has developed a dual sensor for recording object surface's with a diffuse and a direct light at the same time. León and Beyerer [8] proposed a technique where more than two images of the same object recorded with different lighting techniques can be fused in only one image. The major disadvantage of those approaches is of course that they necessitate more than one illumination. The direct consequence is that their integration in the industrial process is more complex and that the data processing chain is more extensive.

In contrast to conventional computing techniques based on a structured illumination, we propose a 2.5D approach using structured light for the purpose of specular cylindrical surfaces inspection. The *deflection* of the light rays is used *without measuring* the deformation of the projected rays in the recording sensor, as this is achieved by deflectometric methods [13].

We propose an algorithmic approach for the automatic discrimination of defective surfaces with structural and textural defects and nondefective surfaces under the constrains of recording artefacts. We demonstrate that it is possible to obtain a high inspection quality, so that the requirements of the automatic classification system of metallic surfaces are fulfilled.

We further emphasize the robustness and the simplicity of the proposed solution as no part of the recording setup (cameras, light projector, object) has to be calibrated. Hence, the aim of this work is

(i) to propose an adapted illumination technique for machine vision applications and so to demonstrate that this lighting is specially adapted to the detection of defects of micrometer depth on specular surfaces of cylinders;

(ii) to show that based on this illumination both structure *and* texture information can be retrieved in one camera recording *without calibration* of the recording hardware;

(iii) to compare the proposed illumination with two other lighting techniques;

(iv) to demonstrate that excellent classification results are obtained using images of surface illuminated with the proposed illumination technique;

(v) to describe and discuss the robustness of the proposed method with respect to artefacts arising from nonconstant recording conditions such as the change of illumination or variations of object positions.

This paper is organized as follows. We first introduce the surface inspection and the corresponding classification problem in Section 2. The recording situation of metallic surfaces under structured stripe illumination is described in Section 3. We compare the proposed illumination technique with a diffuse and a retroreflector approaches in Section 4. The proposed pattern recognition algorithm is described in Section 6, and, in Section 7, based on a large and annotated reference image dataset, we show the results, and discuss our work in Section 8.

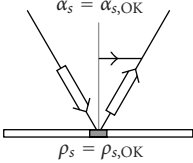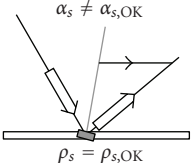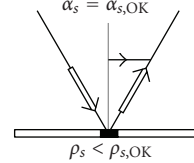## 2. PROBLEM FORMULATION AND TASK DESCRIPTION

Our goal is to automatically discriminate between different metallic object surfaces, for example, as "nondefective" and "defective" while classifying digital images of these surfaces *acquired using structured light* into predefined classes. Defect types are on metallic surfaces manifold as they can be textural defects, structural defects, or a combination of both. In the considered industrial inspection, *long cylindrical* object surfaces such as tubes or round rots of *different diameters* have to be inspected. The automatic inspection should be done at the end of the production line where the objects are moving with a constant speed.

The requirements from the inspection task are twofold. The first aim is to detect *all* the defective surfaces and in the same time to have a *low* false alarm rate. As we consider two kinds of defective surfaces, the structural 3D and the textural 2D, the inspection task considers different *misclassifications rates of 3D in 2D and vice versa.*

Considering the first requirement, the most important condition, as this is the case in most of the automatic inspection systems, is that 100% of the surface defects must be detected. Defects considered within this work are surface abnormalities which can appear during the production. A false positive, (false defect, i.e., a nondefective surface wrongly detected as defect surface), may be tolerated within an acceptable range, expressed in the percentage of the production capacities. Typically, up to 10% of the nondefective surfaces can be classified as defect surfaces. This value has been calculated according to the costs of the manual reinspection of all false-classified objects.

For the second requirement, the inspection task imposes that *structural* defects must be detected and classified

TABLE 1: Influence of the surface type on the reflection angle α and the reflection coefficient ρ. $\alpha_{s,\text{OK}}$ and $\rho_{s,\text{OK}}$ are the reflection angle and reflection coefficient for nondefective surfaces. (a) Nondefective surface, $\rho_s = \rho_{s,\text{OK}}$ and $\alpha_s = \alpha_{s,\text{OK}}$; (b) structural defect. $\rho_s = \rho_{s,\text{OK}}$ is the same as for nondefective surfaces but the surface deformation induces a change of the reflection angle $\alpha_s \neq \alpha_{s,\text{OK}}$. (c) Textural defect. $\alpha_s = \alpha_{s,\text{OK}}$ is the same as for nondefective surfaces but the surface is less reflective which influences the reflection coefficient $\rho_s < \rho_{s,\text{OK}}$.

Surface types		
Nondefective surface	Structural defect	Textural defect
(a)	(b)	(c)
$\alpha_s = \alpha_{s,\text{OK}}$	$\alpha_s \neq \alpha_{s,\text{OK}}$	$\alpha_s = \alpha_{s,\text{OK}}$
$\rho_s = \rho_{s,\text{OK}}$	$\rho_s = \rho_{s,\text{OK}}$	$\rho_s < \rho_{s,\text{OK}}$

correctly with a 100% accuracy, no misclassifications as textural defects are allowed. The reason is that, a distorted surface geometry signifies a change in the functionality of the inspected object. For *textural* defects the situation is different, because they are not a synonym of a functionality change of the inspected object, but correspond to an unclean surface. This is a cosmetic criterium and thus misclassifications as structural defects are not so critical. False classification rates of 2D in 3D defects up to 10% are allowed.

Those conditions define the inspection constraints of the whole inspection system as well as of every element of the processing chain.

The primary information source is the illumination. A great attention should be given in its capability to reveal all the necessary information from the recorded scene. Last element of this chain is the classification result ($\Omega_\kappa \in \{\Omega_A, \Omega_{R,S}$ and $\Omega_{R,T}\}$), where Ω_A is the class of nondefective surfaces, $\Omega_{R,S}$ is the class of structural defects and $\Omega_{R,T}$ the class of textural defects. The image classification procedure is part of the pattern recognition field. The readers can find more details on the description of this field in Niemann [14].

3. PROPOSED ILLUMINATION TECHNIQUE

This section describes the adapted structured illumination technique which is based on the ray deflection on specular surfaces. After a short description of the principle of ray deflection and starting from the exposed problem (see precedent section), we describe step by step the major components of the proposed illumination. We conclude this section by giving some examples of recorded specular surfaces and show that a good enhancement of the visibility of textural and structural defects can be achieved.

3.1. Specular lighting principle

Object inspection using a specular lighting technique is applied for high reflective surfaces with a high value of reflectance coefficient ρ. ρ expresses the percentage of the re-

flected to the projected flux of light. This coefficient is null for diffuse surfaces which reflect the light in any direction, that is, as Lambertian sources. For a specular reflection the angle α of the reflected component is equal to the angle of the incident beam with respect to the surface normal. Compared to defective regions, we consider slowly varying values of α for all inspected surfaces without structural defects.

The disturbances of the projected light pattern are therefore directly linked with the illuminated object surface types. We call (s) an elementary surface element of object surface (S) to inspect. ρ_s and α_s are the reflectance coefficient and the reflection angle of surface element (s). Table 1 uses three examples illustrating ideal reflection conditions of a reflected ray on a surface element (s).

3.2. Adapted specular lighting for the inspection task

As discussed in the introduction, the use of an adapted structured illumination within this work is motivated by the visual inspection process of the human inspector. He turns and moves the high-reflective metallic surface of the object under various and varying illuminations to detect all possible two- and three-dimensional defects. Doing so, he or she is able to recognize surface abnormalities by observing the reflection of a structured illumination onto the surface to inspect.

To emulate this process for machine vision, a specially designed technique for structured illumination has been developed and applied for cylindrical metallic objects. This technique is used in an industrial process as described in Section 2. The image generation process for the proposed structured light depends on three components: the camera sensor (C), the illumination (L), and the physical characteristics (reflectivity and geometry) of the surface (S) to inspect.

In case of the inspection task of high-reflective metallic cylindrical objects, the use of *line-scan sensors* was naturally imposed as the surface of long, constant moving objects has to be inspected. In fact, the *scanning* of the surface, contrary to the pure perspective projection as for matrix-sensors, allows to record the whole surface without a perspective distortion along the longitudinal axis of the objects. Hence, the images recorded with one scanning sensor can directly be stitched together. No preprocessing step for distortion removal is necessary. Each object portion is projected onto the recording sensor along the scanning plane Π_{scan}. The relative position of the recording sensor (C) and the moving direction $\vec{V}$ has a direct influence on the recording distortions. These are negligible when the direction of the line-scan sensor (C) and Π_{scan} are perpendicular to $\vec{V}$ and when the optical axis of the sensor passes through the central axis of the cylindrical object.

An important constraint comes from the high reflectivity of the surfaces to inspect. In fact, the sensor (C) and the light source (L) must be positioned, so that at least one emitted light ray, projected onto a nondefective surface (S), is reflected onto a sensor element. To describe this scene it is convenient to use several coordinate systems. Points on the surface (S) are described in the world coordinate system (x_w, y_w, z_w) whereas points on the acquired images are given

in image coordinate system (u, v). The positions of the major setup components (C), (L), and (S) are schematically depicted in Figure 1.

The object to be inspected is moving along the x_w axis, the sensor (C) is placed so that the line-scan sensor (C) is parallel to the axis y_w and the optical axis pO passes through the central axis of the object. α_{scan} is the angle between planes Π_{scan} and Π_{x_w, y_w}. We choose an α_{scan} near $\pi/2$ to reduce at as far as possible the recording distortions.

Let us now define more precisely the light source (L) which reveals both three- and two-dimensional surface defects. The imperatives are here a *fast moving of the surface* (S) to inspect and a *fast detection and discrimination* of the two- and three-dimensional defects on it. We define $LP_{projected}$ as the projected light pattern onto the surface (S) and $LP_{reflected}$ as the reflected pattern by (S). $LP_{reflected}$ which is disturbed by the object geometry *and* the two- and three-dimensional defects is then projected onto the sensor (C).

Measurement methods of high-reflective surfaces use the deformations of a projected fringe pattern, to retrieve the shape of the surface or detect the defective surface parts.

As specular surfaces reflect the incoming light only in one direction, the size and the geometry of the illumination depend on the shape of the inspected surfaces. In case of free-form specular surfaces with low varying surface vectors, a planar illumination with a reasonable size can be used to inspect the whole object. Knauer et al. [13] use such a system with a flat illumination for the inspection of optical lenses. When the variations of the surface to be inspected are more pronounced, an adapted geometry of the illumination facilitates the recording of the complete surface. Hence, in case of free-form shapes as car doors [15, 16] or the coverage of headlights [17], a parabolic illumination allows to restrain the dimensions of the lighting screen to reasonable values. Different methods using adapted patterns and illumination source shapes are described by Pérard [18].

The structure of the observed fringe patterns in the images is nonregular and depends on the shape of the illuminated surface. Hence, a preliminary calibration step retrieving the geometry of the recording setup is necessary. References [15, 16] compute the mapping between the camera points and the corresponding point on the illumination screen. Knauer et al. [13] use a precalibration procedure to retrieve the position of the camera and the geometry of the structured lighting in the world coordinate system.

Our approach is different. The common part with the existing techniques is that we also adapted the geometry of the lighting to the cylindrical shape of the object under inspection. But, the primary reason was to influence the aspect of the reflected light pattern $LP_{reflected}$ in the camera image. Due to the constant shape of the inspected surfaces, if the geometry of the reflected light pattern is known, the deformations of the fringe pattern induced by a defective object part are sufficient information to automatically detect this surface abnormality. Hence, contrariwise to the above-cited methods, a precalibration step of the recording camera or the structured illumination is not necessary.

Therefore, the structure of the observed pattern is an important aspect concerning the image processing algorithms.
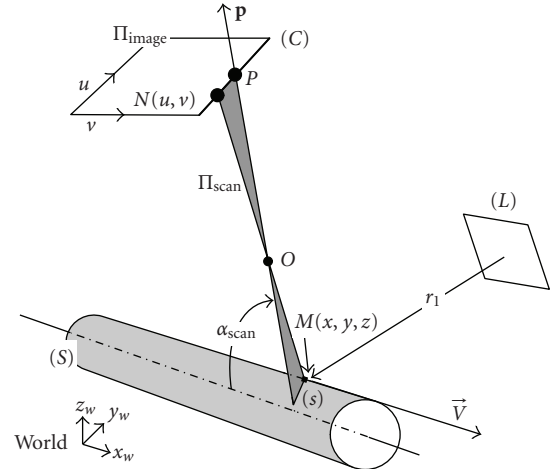

FIGURE 1: Position of the camera line-scan sensor (C), the illumination (L), and the high-reflective cylindrical surface (S). The object is moving with a constant speed V along the x_w axis, the scanning plane Π_{scan} has an angle α_{scan} with the Π_{x_w, y_w} plane. The elementary surface element (s) is characterized by a point M of world coordinate (x, y, z). M is illuminated by a light ray r_1 which is reflected on (s) and projected onto the camera sensor (C) so that the corresponding image point N of image coordinates (u, v) is obtained. The sensor (C) is characterized by the optical center of projection O and the optical axis $\mathbf{p}$. Vector $\mathbf{p}$ passes through the point O and is directed to the point P at the central position of the sensor.

In fact, their complexity and so their processing time may increase with the complexity of the projected light pattern in the recording sensor. Thus, it is preferable to observe a regular pattern in the camera image and so to simplify the image processing procedure. In our case, this reflected observed pattern in the images consists of a vertical, that is, parallel to the image axis v, periodical structure.

Figure 2 shows the arrangement of the N_r projected light rays forming the illumination (L) (which is adapted to the geometry of (S)) and the recording line-scan camera (C). The figure depicts (a) the front view and (b) the side view of the recording setup which consists in the scanning camera (C), the surface to inspect (S), and the illumination (L).

The depicted recording setup shows that with one line-scan sensor (C) and an adapted illumination (L) a large part of the surface $(S_{inspect})$ of the whole surface (S) can be inspected, $(S_{inspect}) \in (S)$. The cylindrical metallic object is moving with a constant speed $\vec{V}$ perpendicular to the line-scan sensor (C). The camera focuses near to the object surface. The depth of field is chosen to be sufficient to cover the whole curved surface $(S_{inspect})$. The number N_r of necessary light rays depends on the lateral size (along the y_w axis) of the inspected surface $S_{inspect}$ and the minimal size of the defects to be detected.

Figure 2(a) shows that the arrangement of the projected light pattern $LP_{projected}$ is calculated according to the cylindrical geometry of the object surface, so that the reflected light pattern $LP_{reflected}$ on the surface $S_{inspect}$ is projected onto the sensor (C) as a vertical and periodical pattern in the scanning plane Π_{scan} of the camera.
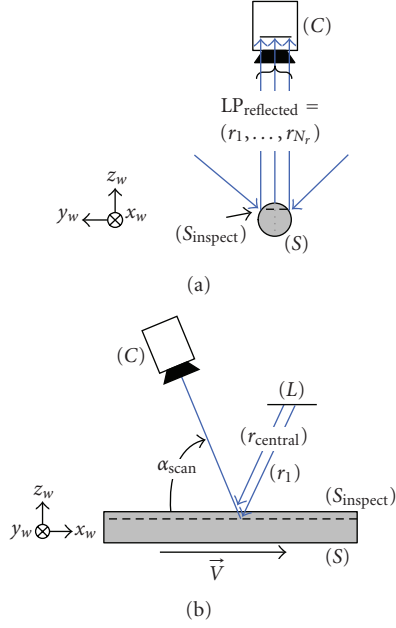
FIGURE 2: Principle of adapted structured illumination for the inspection of high-reflective surfaces of cylindrical objects, (a) front view and (b) side view. The cylindrical object is scanned during its movement with constant speed V by a line-scan sensor (C). $(S_{inspect})$ is the part of the surface of (S) that is inspected with one camera and one illumination. N_r light rays $(r_1, \ldots, r_{N_r})$ are necessary to cover the whole surface $(S_{inspect})$.

Figure 2(b) depicts the reflection of two rays reflected by the object surface $(S_{inspect})$ and projected onto the camera sensor (C): the central light ray $r_{central}$ and one extreme ray r_1. We clearly see that the N_r projected rays onto $(S_{inspect})$ are not coplanar because we have chosen a scanning angle $\alpha_{scan} < \pi/2$.

After describing how the N_r rays forming the illumination are to be projected onto the surface, we detail more precisely the different parts forming this adapted structured illumination (L). Figure 3 shows the Lambertian light (D), the light aperture (A_L), and the ray aperture (A_R).

The adapted illumination for the structured light itself is composed of three parts: a Lambertian light source (D), a light aperture (A_L), and a ray (A_R) aperture.

Aim of the Lambertian light (D) surrounding the surface to inspect (S) is to create a smooth diffuse illumination to reduce disturbing glares on the metallic surface due to its high reflectivity.

A part of the light rays emitted by (D) is passing the N_r slits of the ray aperture (A_R). We assume that all the slits have the same length L_s and the same width w_s. A certain length L_s is necessary as we know that the emitted rays which are then projected into the sensor (C) are not coplanar; see Figure 2(b). This length depends on the scanning angle α_{scan} and the diameter of the cylindrical object to inspect D_O. The width w_s depends on the necessary lateral resolution along the y_w axis which is given by the projected pattern $LP_{reflected}$ into the camera sensor (C). As this pattern has a sinusoidal structure of period $d_{P,mm}$, the width $w_s = d_{P,mm}/2$.

The light aperture (A_L) is placed behind (D) to retain all light, except the light rays needed to form the fringe pattern.

The depicted illumination in Figure 3 is one possible method to project a periodical stripe pattern onto the sensor. Similar images could have been obtained with a screen projecting a sinusoidal pattern. In that case, an intermediate reflecting element would have been necessary to adapt the planar light structure to the geometry of the cylindrical surfaces. The proposed solution has the advantage to be easy to manufacture, to be cheap, and to have reasonable dimensions.

As the whole surface (S) cannot be recorded with one camera, $(S_{inspect}) < S$, several cameras and corresponding adapted structural illuminations must be used for covering the complete circumference of a metallic cylinder. The number N_C of needed cameras depends not only on the diameter of the object D_O, the width of the ray aperture's slits w_S but also on the distance between the surface to inspect and the recording sensor. Figure 4 illustrates this statement by showing the reflection of the extreme light ray r_1 and the cental light ray $r_{central}$ onto the sensor (C).

This example shows that the lateral size of the inspected surface using the adapted structure illumination depends on the following parameters: D_O, w_S, and distance between $(S_{inspect})$ and (C). From the lateral size of the surface $(S_{inspect})$, the number N_C of needed cameras to record the whole surface (S) can be deduced.

3.3. Image examples of recorded nondefective surfaces

The recording setup is operable if the image of the projected light pattern $LP_{reflected}$ is characterized by a succession of vertical parallel and periodical bright and dark vertical regions. This vertical pattern has to have a constant period $d_{P,px}$ (in pixel) in the u direction of the image. The ratio of $d_{P,px}$ with the period $d_{P,mm}$ (in millimeter) of the pattern $LP_{reflected}$ gives the image resolution in u direction of the image coordinate system.

An image example of a cylindrical tube surface section illuminated with the proposed structured lighting is shown in Figure 5.

Here, $N_r = 21$ rays are necessary to illuminate the complete cross section of the surface $(S_{inspect})$. In this image, one single horizontal image line corresponds directly to the scan line of the line-scan sensor at a certain point of time t. Thus, the depicted image is obtained by concatenating a certain number of single line scans, where the vertical resolution v corresponds directly to the number of line scans over a certain period of time. All the N_r bright stripes in the image $\mathbf{f}$ are vertical (along the v axis) and parallel to the moving direction of the cylindrical object; see Figure 2.

The recording conditions are optimal for the further processing and classification. By optimum, we mean that the observed stripe pattern in the image must be depicted *vertically*, with a *constant period* and that all bright lines in the image are depicted with the *same pixel values*. The image processing algorithms should not be perturbed by any recording noise present in the image. We distinguish two recording
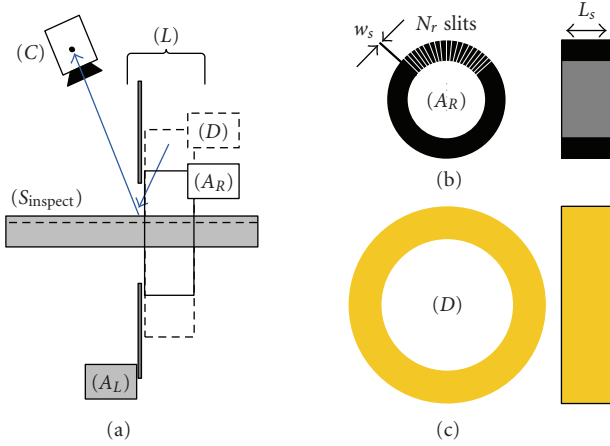
FIGURE 3: Detailed principle of the adapted structured illumination for the inspection of high-reflective surfaces of cylindrical objects. The adapted structured illumination is composed of a ray aperture (A_R), a Lambertian diffuse light (D), and a light aperture (A_L). (a) Side view of the whole illumination, (b) front and side views of the ray aperture (A_R), and (c) front and side views of the Lambertian diffuse light (D).
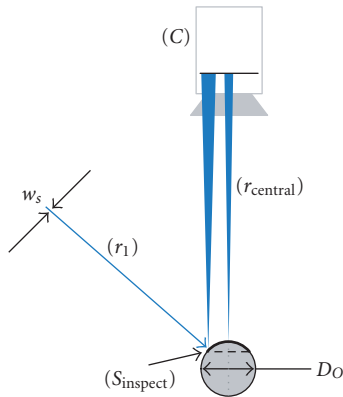

FIGURE 4: Projection of the extreme light ray r_1 and the cental light ray $r_{central}$ onto the sensor (C) using the adapted structured illumination. As each slit of the ray aperture A_R has the same width w_s, the reflected rays on the surface are more or less spread, depending on the diameter of the object D_O and the distance between the surface to inspect and the recording sensor. Here is the example of the projected extreme light ray r_1 and cental light ray $r_{central}$ onto the sensor (C).

noise categories. The first is the unavoidable but uncritical camera noise due the electronic devices of the camera. The second is due to the geometry of the object and the illumination as stated according to Figure 4. The second kind of recording noise can clearly be seen with a close look at the stripe image of Figure 5 where we observed a decrease of the contrast for the left and right vertical stripes.

To summarize, for every illuminated elementary surface (s) of the nondefective surface $(S_{inspect})$, we have ideal reflection coefficients $\rho_s = \rho_{s,OK}$ and ideal reflection angles $\alpha_s = \alpha_{s,OK}$; see the left image of Table 1. We fix the ideal reflection coefficient to be maximal, that is, $\rho_{s,OK} = 100\%$. This
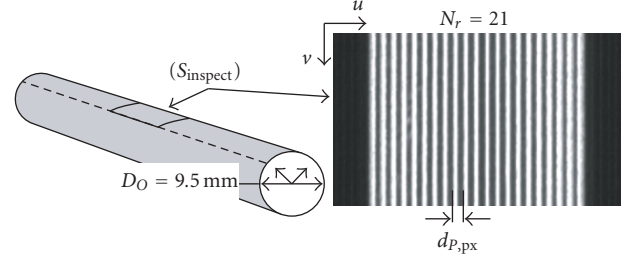

FIGURE 5: Typical image of a specular *nondefective* cylindrical surface of diameter $D_O = 9.5$ mm obtained with the adapted structured illumination. $d_{P,px}$ is the period in pixel of the depicted stripe pattern in the image.

corresponds to the maximal value in the images, the intensity value of the vertical bright stripes therefore always equals 255, which is the maximal possible value as the depth of all the considered images is of 8 bits.

As defined in Figure 5, for the recording of the surface we need at least $N_c = 6$ adapted illuminations and cameras to record and inspect the complete surface (S) of the cylindrical object.

3.4. Revealing textural and structural defects

The goal of the described recording setup is to emulate the inspection process of a human visual inspector, to accentuate both two- and three-dimensional defects on the object surface at the same time. We saw in Figure 5 how nondefective surfaces are depicted, let us now have a look on depicted textural and structural defects on cylindrical metallic surfaces recorded under the proposed illumination; see Figure 6.

Considering these height image examples, we observed that different types of defects (textural and structural) induce a different kind of stripe disturbances. For textural defects, mainly the intensity of the adapted stripe illumination decreases. This can even lead to the effect that neighboring dark and light regions are melted; see Figures 6(a1)–6(c1). However, for structural defects, the parallel structure of the stripes is deformed or vanished; see Figure 6(d2).

In our four textural defects examples, we see that the corresponding image disturbances are due to a decrease of the reflected intensity. This means that the reflection coefficients of all the elementary surfaces (S) characterizing those two-dimensional defects are lower than the reflection coefficients of nondefective surfaces $\rho_s < \rho_{s,OK}$. This is therefore a sufficient condition to reveal this kind of defects in the images.

Concerning the four structural defects examples, the situation is slightly different. We observe naturally a deformation of the projected vertical stripes in the image which is due to a change in the reflection angle, $\alpha_s \neq \alpha_{s,OK}$. However, we also observed a decrease in the intensity of the projected stripes. First, when the texture of the surface is damaged, we have the same conditions as for textural defects, that is, $\rho_s < \rho_{s,OK}$; see the inner part of the "3D wear" and "3D abrasion" defects. Then, a shape deformation of the surface can also lead to a decrease of bright stripes intensity, see the

"2D grease"
(a1)

"2D scratch"
(b1)

"2D rough"
(c1)

"2D mark"
(d1)

"3D hit"
~20 μ depth
(a2)

"3D wear"
~20 μ depth
(b2)

"3D cavity"
~20 μ depth
(c2)

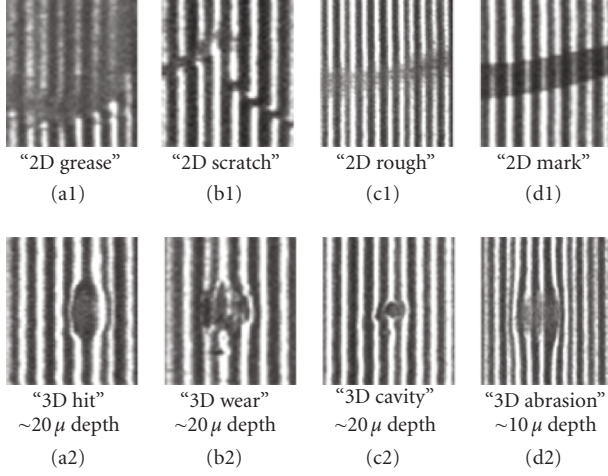"3D abrasion"
~10 μ depth
(d2)

FIGURE 6: Image examples of different surface defects recorded with the adapted structured illumination. (a1) the "2D grease" figure shows a grease mark on the surface; (b1) the "2D scratch" depicts a lightly scratched surface; (c1) "2D rough" is due to an abrasion of object surface during surface finishing process; (d1) a typical marking on the surface is depicted in image "2D mark." Four image examples of different depth defects. (a2) "3D hit" reveals a strong damaged surface, (b2) "3D wear" is due to the mold of an external particle on object surface, (c2) "3D cavity" is due to the pressing of an external object on the surface, and (d2) "3D abrasion" shows a strongly locally polished surface.
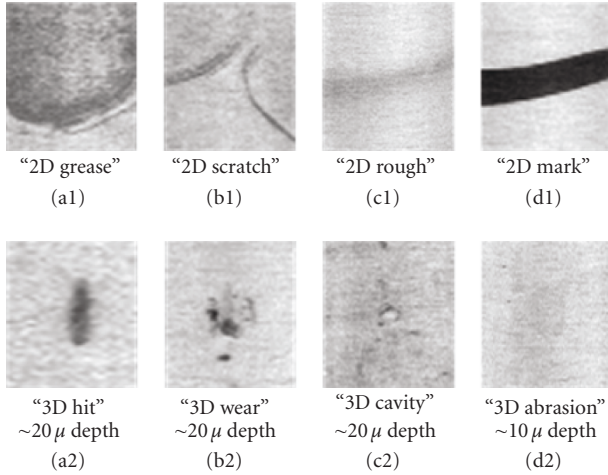

"2D grease"
(a1)

"2D scratch"
(b1)

"2D rough"
(c1)

"2D mark"
(d1)

"3D hit"
~20 μ depth
(a2)

"3D wear"
~20 μ depth
(b2)

"3D cavity"
~20 μ depth
(c2)

"3D abrasion"
~10 μ depth
(d2)

FIGURE 7: Image examples of different surface defects recorded with a diffuse illumination. Same textural "2D grease," "2D scratch," "2D rough," "2D rough" and structural "3D hit," "3D wear," "3D cavity" "3D abrasion" images as shown in Figure 6.

disturbed stripes at the borders of the "3D hit" and "3D abrasion" defects. We observe that those bright stripes follow the contours of the defects where the angle of the surface normal changes in the lateral y_w direction (see Figure 2(a)). If the angle of the surface normal changes in the longitudinal $(x_w; z_w)$ direction (see Figure 2(b)) less light flux is projected onto (C) so that the intensity of the bright stripes in the image decreases.

Hence, a variation of the surface normal without a change of the reflection coefficient, which is characteristic to a structural defect, can lead to similar disturbances in the stripe image than a textural defect would induce. See, for example, the inner parts of the "3D abrasion" image and the "2D rough" image of Figures 6(d2), 6(c1). The direct consequence is that, if *all* the variations of the surface normal of a structural defect *only* occur in the plane $(x_w; z_w)$, then this defective structural surface would not be distinguishable from a textural defective part.

This particular case of structural defect structure has a very low probability to occur as in case of the inspection task, all structural defects to detect have an irregular and random structure. This illumination technique is therefore totally adequate for the visual enhancement and discrimination of textural and structural defective parts of cylindrical surfaces as it will be demonstrated in the next sections.

4. COMPARISON OF THE PROPOSED METHOD WITH TWO DIFFERENT ILLUMINATION PRINCIPLES

The described recording setup is one possible illumination technique among several others, used in industrial image processing and machine vision systems.

To demonstrate that the proposed adapted stripe illumination integrates two different illumination techniques (diffuse and directed) for the detection of textural and structural defects, we performed further recordings of the high-reflective surfaces described in Section 3. We use a *diffuse* and a *retroreflector* illumination technique. We show that the former does not increase the visibility of all the structural defects whereas the latter is too sensible to the nondefective surface structures.

4.1. Use of a diffuse illumination technique

First recordings with the involved high-reflective surfaces were made using a smooth diffuse illumination. The purpose was to increase the visibility of textural changes of the surface and to evaluate the enhancement possibilities for structural defects.

A concrete idea of the surface texture enhancement possibilities using a diffuse technique is given in Figure 7 where the same eight metallic surfaces as showed in Figure 6 with the adapted structured illumination are depicted. Figures 7(a1)–7(d1) depict textural defects whereas Figures 7(a2)–7(d2) depict structural defects.

Obviously, the surfaces exhibiting textural defects demonstrate that a smooth illumination is fully appropriate for revealing defective object textures whose reflectivity is less than nondefective surfaces textures. Interestingly, the figures depicting textural defects show that also depth structures can be revealed with this kind of illumination technique. The necessary condition is that the surface reflectivity of the defect differs from the reflectivity of good surface. But the major drawback of this illumination is that some structural defects, in particular those with a small depth (see Figure 7(d2)), are quasi-invisible in the images.
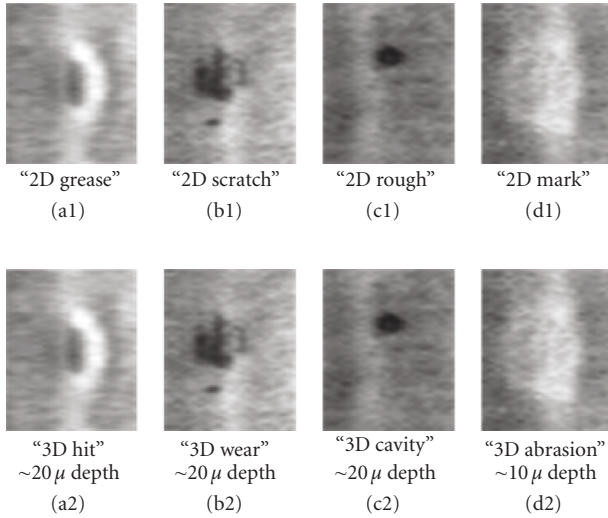
"2D grease"   "2D scratch"   "2D rough"   "2D mark"
    (a1)   (b1)   (c1)   (d1)

"3D hit"   "3D wear"   "3D cavity"   "3D abrasion"
$\sim 20\mu$ depth $\sim 20\mu$ depth $\sim 20\mu$ depth $\sim 10\mu$ depth
    (a2)   (b2)   (c2)   (d2)

FIGURE 8: Image examples of different surface defects recorded with a retroreflector. Same textural "2D grease," "2D scratch," "2D rough," "2D rough" and structural "3D hit," "3D wear," "3D cavity" "3D abrasion" images as shown in Figure 7.

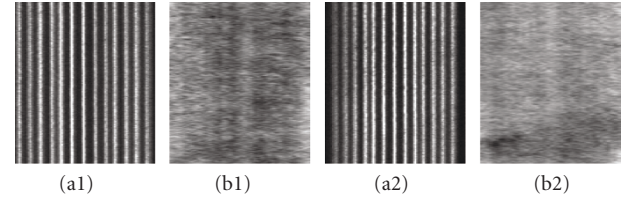(a1)   (b1)   (a2)   (b2)

FIGURE 9: Image examples of two different nondefective surfaces. (a1) and (b1) depict the same nondefective surface recorded with a structured and a retroreflector lighting, (a2) and (b2) depict another nondefective surface recorded with a structured and a retroreflector lightings.

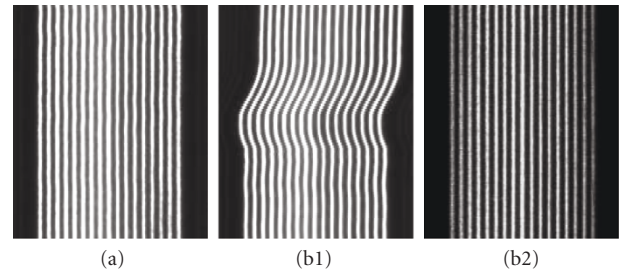(a)   (b1)   (b2)

FIGURE 10: Image examples with typical recording artefacts due to bad-positioned objects. (a) ideal depiction of a nondefective surface, the stripe pattern in the image is not disturbed; (b1) change of object position in the y-direction during surface recording, (b2) bad-positioned object corresponding to a rotation around the y-axis.

The eight images examples (Figure 7) illustrate the importance of a smooth illumination when textural defects have to be detected on high-reflective surfaces, and also demonstrate the limits of a diffuse illumination when depth structures have to be revealed. In fact, when the texture of the defect has a similar reflectivity as a nondefective surface, as in Figures 7(c2) or 7(d2) the defect is quasi-revealed not revealed in the images.

Therefore, this illumination approach is not suitable to the inspection task as defined in Section 2.

4.2. Use of a retroreflector illumination

One of the first applications of the retroreflector technique for the quality inspection of specular surfaces was proposed by Marguerre [11]. He showed that this technique is particulary adapted for the enhancement of small surface deformations and presents his method as a good possibility to enhance three-dimensional surface structures or surface regions with different specular properties.

We tested this approach to evaluate how far this method is suited for the inspection of our high-reflective surfaces. We record the same textural and structural defects as depicted in Figures 6 and 7. The results are shown in Figure 8.

At first sight, the two major defect types which are the textural and the structural are well enhanced. The images of the former are similar to the results obtained with the diffuse technique whereas the latter are also well enhanced, which was not the case using the "smooth" illumination. So, this approach seems to give satisfying results concerning the increase of nondefective surfaces as for the proposed structured lighting technique; see Figure 6.

In fact, the obtained images using this technique are similar to the conclusions of Marguerre [11]. He says that placing a retroreflector in the optical setup is equivalent to high-

pass filtering the resulting images without retroreflector. To be sure if this method is suitable for our inspection purpose, we made further tests by recording nondefective surfaces; see Figure 9.

We highlighted that the retroreflector technique is a highly sensitive method. Even in the case of nondefective surfaces, high grey level variations can be observed in the images. Contrariwise, the images of the same surfaces obtained using the proposed illumination do not show these perturbations.

The textural defects seem to be well visually enhanced with the retro technique, a discrimination with textural defect is not possible. Figures 8(b2) and 8(c2) clearly demonstrate that textural defects can be depicted with similar grey values than textural surfaces.

5. DIRECT APPLICATION IN AN INDUSTRIAL ENVIRONMENT

We proposed a new lighting technique for specular surfaces inspection by visually enhancing the textural and structural defects without revealing nondefective surfaces in the same time. We compared our results with a diffuse and a retroreflector lighting technique and showed that for both techniques the results are not as good as for the proposed adapted stripe illumination.

Now we aim at demonstrating that such a lighting system can be used in an industrial environment where the system's
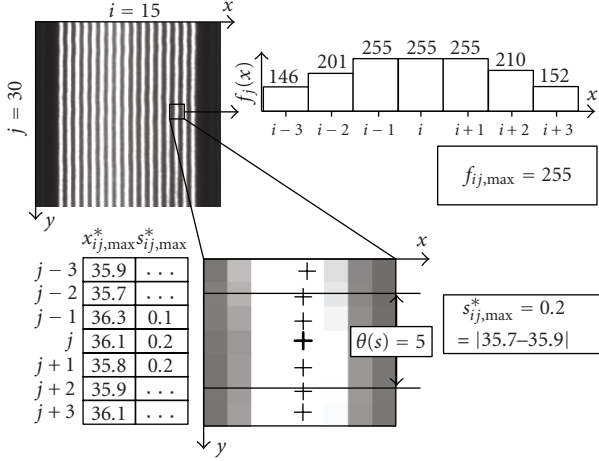
FIGURE 11: Determination of the shape $s^*_{ij,\max}$ and the intensity $f_{ij,\max}$ values at maximum position $x^*_{ij,\max}$ for a stripe image. The determination of those three parameters is done for maxima at positions $i = 5$ and $j = 30$. The shape $s^*_{ij,\max} = 0.02$ and the intensity $f_{ij,\max}$ values correspond to optimal recording conditions, that is, when nearly no bright stripe disturbance occurs.

constraint is not only to achieve a high inspection's quality *but also* to reach a high productivity. It is therefore quasi-not possible under those conditions to obtain a constant image quality of the recorded surfaces. We show two typical examples of artefacts arising when the recording conditions are not optimal.

We briefly introduce the involved algorithm for the automatic segmentation and classification of structural and textural surface defects illuminated with this specular lighting. We show that the proposed method is robust against recording artefacts and that a good discrimination between nondefective surfaces, textural defects, and structural defects is possible.

5.1. The problem of specular lighting's artefacts

The images shown in Section 3 clearly demonstrated the strength of the proposed illumination for surface characterization. Up to here, we only consider the stripe disturbances caused by critical surfaces, we did take into account possible image artefacts arising when specular surfaces are illuminated with directional light.

When the recording conditions of object surface are optimal, the quality of the stripe pattern is similar to the depicted surface in Figure 10(a). If not, that is, when recording artefacts occur, the bright lines are disturbed, as it can be seen in Figures 10(b1)-10(b2).

Each of those two artefacts identify one consequence of nonoptimal positioned object surface. Stripe pattern of Figure 10(b1) shows similar properties to the disturbances caused by structural defects, when $\alpha_s \neq \alpha_{s,OK}$, whereas the disturbances induced by textural defects, when $\rho_s \neq \rho_{s,OK}$, are close to those observed in Figure 10(b2).

Causes for such types of disturbances are usually inevitable uncorrect or imperfect recording conditions. Typi-

cal disturbances are short lateral deviations in y-direction of the inspection object with respect to a fixed geometry between object, sensor, and illumination, leading to a short-term horizontal distortion in the depicted stripe pattern. See Figure 10(b1) where the complete bundle of reflected rays (R) is displaced in the image. Also, a bad-positioned or dejustified object with respect to the image sensor can yield to inhomogeneous illuminated surfaces and thus wrong conditioned images. In Figure 10(b2), the plane defined by the reflected ray bundle (R) does not correspond to the projection plane of the recording sensor.

5.2. Quantifying image quality

The ideal recording conditions as defined in Section 3.3 cannot be fulfilled at 100% in an industrial context. The recording artefacts characterized by a shape distortion and/or an intensity decreasing of bright lines are quasi-unavoidable. To evaluate the influence of such artefacts on the discrimination process of nondefective and defective surfaces, we must quantify the *quality* of the depicted stripe pattern in an image. Two criteria are here important: the *shape* and the *intensity* of the bright lines.

The question is "how far can recording artefacts disturb the projected stripe pattern, so that the surface inspection process is still acceptable?".

To answer this question, we must quantify the shapes and the intensities of the depicted bright lines in an image **f**. Those values, both calculated from the picture elements of the images, will help us to evaluate the degree of bright lines disturbance.

Each image **f** of size $N_x \times N_y$ is characterized by N_l vertical bright lines depicted with a period $d(P)$. The function $f(x, y)$ is the two-dimensional discrete representation of **f** and is represented in a cartesian coordinate system whose x-axis is horizontal with ascendant value from left to right and y-axis is vertical with ascendant values from top to bottom. Upper-left image point at pixel position $(0, 0)$ of $f(x, y)$ corresponds to the origin of the coordinate system.

At first, we estimate the $N_y \times N_l$ positions of all N_l bright lines. We call those positions the maxima $x^*_{ij,\max}$ of the image **f**, $i = 1, \ldots, N_l$ defines the bright line number and $j = 1, \ldots, N_y$ the position along image's y-axis. All maxima $x^*_{ij,\max}$ are estimated with a high accuracy in x-direction.

One major problem concerning the detection of the maxima is that most of the brightest points are mapped to a value of 255. This clipping is unavoidable, as high-reflective surfaces are involved. Hence, for the detection of the maxima at subpixel level $x^*_{ij,\max}$, we implemented and compared two different methods: the center-of-mass and the Blais-and-Rioux operators. The first uses the distribution of the grey level to retrieve the positions of the maxima, whereas the second applies a local linear interpolation at the zero-crossing of the first derivative. Both methods are detailed described in Fisher and Naidu [19].

We have conducted several tests using synthetic image with a simulated additive noise and different maxima corresponding to grey values comprised between 220 and 255. Further tests involving real images have also been made.

Concerning the synthetic images, the evaluation criterion was the detection error between the estimated and the known maxima positions. For the real images, we used the classification rates as evaluation criterion. Both series of tests showed that the grey level distribution center-of-mass method outperforms the zero-crossing Blais-and-Rioux approach.

Once the maxima $x^*_{ij,\max}$ are computed, we calculate the corresponding shape $s^*_{ij,\max} \in \mathbb{R}$ and intensity values $f_{ij,\max} \in \mathbb{Z}$. Figure 11 shows the computing principle for image function $f(x, y) \in \mathbb{Z}^{64 \times 64}$ of shape $s^*_{ij,\max}$ and intensity $f_{ij,\max}$ values of maxima $x^*_{ij,\max}$ for $i = 5$ and $j = 30$ ($f_y(x)$ is the one-dimensional discrete representation of a horizontal image line of length N_x).

The computation of the $N_y \times N_l$ shape values $s^*_{ij,\max}$ for each $x^*_{ij,\max}$ can be stated as follows:

$$s^*_{ij,\max} = \begin{cases} |a_1 - a_2| & \text{if } |a_1 - a_2| < \theta(\epsilon), \\ & |a_1 - a_2| = 2\theta(s) + 1, \\ & a_1 = x^*_{i(j+\theta(s)),\max}, \\ & a_2 = x^*_{i(j-\theta(s)),\max}, \\ 0 & \text{otherwise,} \end{cases} \quad (1)$$

$\theta(s)$ and $\theta(\epsilon)$ are threshold values depending on bright stripe's shape and period $d(P)$. The shape value $s^*_{ij,\max}$ is computed using two subpixel positions $x^*_{i(j-\theta(s))\,\max}$ and $x^*_{i(j+\theta(s)),\max}$ of a bright stripe so that $|x^*_{i(j+\theta(s))\,\max} - x^*_{i(j-\theta(s)),\max}| < \theta(\epsilon) < d(P)$. Shape value is minimal when no bright stripe disturbances occur, $s^*_{ij,\max} = 0.2$ for the example given in Figure 11.

Bright line's intensities $f_{ij,\max}$ at maxima $x^*_{ij,\max}$ are the corresponding value of image function $f(x, y)$. Figure 11 represents the ideal case when $f_{ij,\max} = 255$.

The bright stripe disturbances of a complete image or an image region are characterized with $\hat{S}$ and $\hat{I}$, the mean values of maxima's shape $s^*_{ij,\max}$ and intensity $f^*_{ij,\max}$ of this image or this image region. Both expressions are written as follows:

$$\hat{S} = \frac{1}{N_l \times N_y} \sum_{s=1}^{N_l} \sum_{j=1}^{N_y} s^*_{ij,\max},$$

$$\hat{I} = \frac{1}{N_l \times N_y} \sum_{i=1}^{N_l} \sum_{j=1}^{N_y} i^*_{ij,\max}. \quad (2)$$

The average shape $\hat{S}$ and average intensity $\hat{I}$ values of bright lines give us an estimation of their disturbance degree. As an example, Table 2 lists the values of $\hat{S}$ and $\hat{I}$ of the three stripe image examples depicted in Figures 10(a), 10(b1), and 10(b2).

5.3. *Influence of artefacts on classification performances*

We know that recording artefacts are quasi-unavoidable for the target industrial context. Therefore, the classification

TABLE 2: Values of average shape $\hat{S}$ and intensity $\hat{I}$ for the three images depicted in Figures 10(a), 10(b1), and 10(b2).

	Figure 10(a)	Figure 10(b1)	Figure 10(b2)
$\hat{S}$	0.14	1.18	0.16
$\hat{I}$	254	252	200

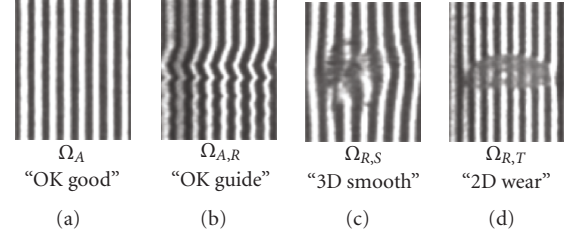|			
Ω_A	$\Omega_{A,R}$	$\Omega_{R,S}$	$\Omega_{R,T}$
"OK good"	"OK guide"	"3D smooth"	"2D wear"
(a)	(b)	(c)	(d)

FIGURE 12: Four stripe images of dimension 64×64 pixels. Those images are part of set w_{te} and were recorded by the visual inspection system. The two first images depict nondefective surfaces: (a) image with good quality without any artefact, (b) disturbed stripes corresponding to mechanical, that is, recording artefacts. The two last images depict (c) a superficial structural defect $\sim 10\,\mu$m and (d) a textural defect corresponding to a "wear" of the surface.

method used for discriminating defective from nondefective surfaces must not be perturbed by nonoptimal recording conditions. How far artefacts can influence the inspection performances and how far they may represent an additional difficulty for the discrimination task will be discussed in this section.

We consider a test image sample w_{te} made of 188 images depicting typical surfaces recorded by the industrial system. All reference images have been used for the qualification of the system and were classified by a visual inspector in four main image sets. We have 40 nondefective surfaces without artefacts w_A and 62 nondefective surfaces with recording artefacts $w_{A,RA}$, 51 nonefective surfaces with structural defects $w_{R,S}$, and 35 nondefective surfaces with textural defects $w_{R,T}$.

Figure 12 gives an example of some typical object surfaces. All images correspond to an object surface of 2 mm width and 6 mm height and are part of the test set w_{te}. Resolution in x direction is three times greater than the resolution in y direction, so that all images have square dimensions of 64×64 pixels.

The depicted stripe images give an example of typical object surfaces to inspect. For each of the four considered defect sets $\{w_A, w_{A,R}, w_{R,S}, w_{R,T}\}$, one example is shown. Figures 12(a) and 12(b) show nondefective surfaces. In the former, no disturbances occur and in the latter typical guiding disturbances are depicted. A structural defect is shown in Figure 12(c), the depth is about $10\,\mu$m and is due to a crushing of the object. Size of "3D deep" defect is relatively big with ~ 7 disturbed periods in x direction. Figure 12(d) depicts one textural defect due to the grating of the tube surface with an object.

We compute the average shape $\hat{S}$ and intensity $\hat{I}$ values as defined by (2) for all images of subsets w_A and for the
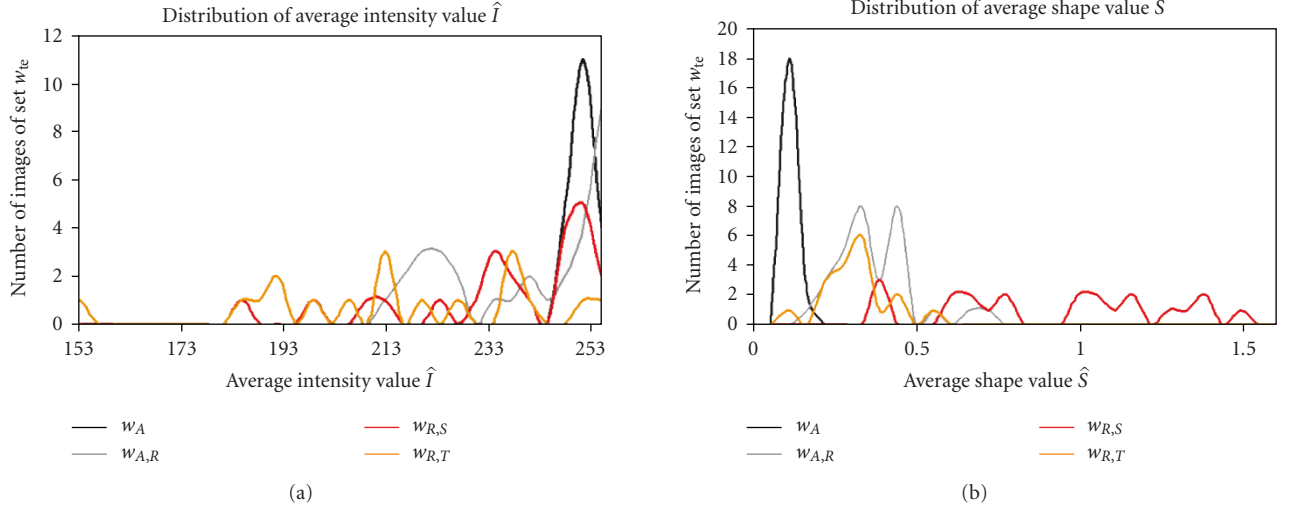
FIGURE 13: Distribution of average shape $\hat{S}$ and intensity $\hat{I}$ values for all images of subsets w_A and for the disturbed image regions of subsets $w_{A,R}$, $w_{R,S}$, and $w_{R,T}$, where $w_{\text{te}} = \{w_A, w_{R,S}, w_{R,S}\}$.

$$
\begin{aligned}
&if \quad (d_2({}^{\varrho}\mathbf{c}; \mathbf{c}) \leq d_2({}^{j}\mathbf{c}; \mathbf{c})), \\
&\qquad ({}^{j}\mathbf{c} \in \Omega_{\kappa}), \\
&then \quad (\mathbf{c} \in \Omega_{\kappa}), \\
&\qquad {}^{\varrho}\mathbf{c} \in R^{N_{\text{tr}}}, \quad {}^{j}\mathbf{c} \in \\
&R^{N_{\text{tr}}}, \quad \mathbf{c} \in R^{N_{\text{te}}}, \\
&\qquad \forall \kappa \in \{1, \ldots, 3\}, \\
\\
&\forall \varrho \in \{1, \ldots, j-1, j+1, \ldots, N_{\text{tr}}\}, \\
&\qquad \forall j \in \{1, \ldots, N_{\text{tr}}\}.
\end{aligned}
$$

ALGORITHM 1: i

disturbed image regions of subsets $w_{A,R}$, $w_{R,S}$, and $w_{R,T}$. The values of $\hat{S}$ and $\hat{I}$ are reported in Figure 13.

Those two Graphes clearly illustrates two items. First, the average values $\hat{S}$ and $\hat{I}$ of defect surfaces, sets $w_{R,S}$ and $w_{R,T}$, and nondefective surface without artefacts, set w_A, are nearly disjoint. Second, the distribution of shape and intensity values $\hat{S}$ and $\hat{I}$ for the nondefective surface with recording artefacts set $w_{A,R}$ covers the whole range of values, a clear threshold separating nondefective from defective surfaces here is not obvious. The fact is that recording artefacts dramatically complicate the classification task consisting in discriminating nondefective and defective surfaces. Bright lines shape and intensity seem to represent good but not sufficient characteristics to solve this discrimination task.

We illustrate the classification difficulty by introducing a shape $\gamma_S = 0,18$ and an intensity $\gamma_I = 246$ threshold. We consider an image as depicting a nondefective surface if its average shape value $\hat{S}$ is bellow γ_S or if its average intensity value $\hat{I}$ is above γ_I. In this case, we classify all 20 images of set $w_{\text{te},A}$ as non-defective surfaces and only 1 image of set $w_{\text{te},R,S}$ as a nondefective surface also. But in the same time we would falsely classify nearly all images of set $w_{\text{te},A,RA}$ as

defective surfaces. In the same way, we classify most of the images of set $w_{\text{te},A}$ as nondefective. The major problem in this case is that images of set $w_{w,RA}$ have similar values of $\hat{I}$ as images of sets $w_{w,3D}$ and $w_{w,2D}$.

This concrete example demonstrates that other characteristic stripe features have to be defined, which brings us to the proposed classification algorithm.

6. THE PROPOSED PATTERN RECOGNITION ALGORITHM

If the proposed specular lighting technique shows good results in visually enhancing critical surfaces, its application in an industrial environment induced nonoptimal recording conditions. This leads to image disturbances similar to those induce by surface defects so that the discrimination task becomes more difficult.

To overcome this problem, an adaptive algorithm was developed for the automatic inspection of structured illuminated surfaces. This method shows its robustness as it is part of a widely used real-time industrial application.

The core component of the algorithm is the selection and the extraction of the features best describing the image contents. The first step of the algorithm consists in building the feature vector $\mathbf{c} \in \mathbb{R}^{N_c}$ for all stripe image pattern $\mathbf{f}$. This process filters the most irrelevant information, transforming an image of size $N_x \cdot N_y$ into its signature $\mathbf{c}$ of dimension N_c, where $N_c \ll N_x \cdot N_y$. The feature vector building process is made of different steps, each one corresponding to a dimensionality reduction.

First, *maxima* and *minima* datasets containing the position of bright and dark image lines are built from the image pattern $\mathbf{f}$. For all image maxima and minima the shape, see (1), the distancem, and the intensity values of bright and dark lines are computed.

Then, only image *regions* corresponding to characteristic shape, distance, and intensity values of bright and dark lines are retained in sets $\mathbf{M}_{R,\text{max}}$ and $\mathbf{M}_{R,\text{min}}$.

Finally, further image regions englobs the regions defined by $\mathbf{M}_{R,\text{max}}$ and $\mathbf{M}_{R,\text{min}}$ are built. Those segmented image regions define the relevant information and so the feature vector $\mathbf{c}$.

For the classification procedure, we consider three classes: the class of nondefective surfaces Ω_A grouping the nondefective surfaces recorded with and without artefacts, the class of structural defects $\Omega_{R,T}$, and the class of textural defects $\Omega_{R,T}$. The task then consists in assigning a class $\Omega = \{\Omega_A, \Omega_{R,T}, \Omega_{R,S}\}$ to each pattern $\mathbf{f}$ according to feature vector $\mathbf{c}$. In addition to the test set w_{te} defined earlier, we consider a *training set* w_{tr} made of 116 images, $w_{\text{tr}} \bigcap w_{\text{te}} = \varnothing$.

The classification scheme we used is a supervised learning one, the class of each pattern $\mathbf{f} \subset w_{\text{tr}}$ and $\mathbf{f} \subset w_{\text{te}}$ is known. From the possible statistical learning approaches or *decision rules* we decide to chose one of the most popular approaches and easy to implement methods: the nearest-neighbor classification (k-NN) (Yang and Liu [20] refers to the k-NN rule as one of the most efficient methods). This is a reasonable approach as our aim is to compare different feature extraction methods for stripes images and not to test and to optimize different classifiers. The k-nearest neighbor (k-NN) technique assigns a feature vector $\mathbf{c} \in R^{N_{\text{te}}}$ from test set w_{te} to the class Ω_κ of the majority of its k-nearest-neighboring image patterns from training set w_{tr}. We consider *one* nearest neighbor $k = 1$ and use the euclidian distance d_2 as metric space for feature vectors pairs. Mathematical expression of k-NN can be stated as shown in Algorithm 1.

The classification algorithm consists of an initial training phase using images of set w_{tr} to define the optimal parameters adjustment. Then classification performance is measured with the test set w_{te} while comparing the true state with the detected state.

7. CLASSIFICATION RESULTS

The classification is done using the images of set w_{te} with the optimized parameters of the algorithm. We would like to underline that we have tried to make this test set as representative as possible. The number of images of sets w_A, $w_{A,R}$, $w_{R,S}$, and $w_{R,T}$ is proportional to the number of images that are classified by the industrial system and the proportion of badly depicted stripes, that is, with a low quality, corresponds to real recording condition.

The parameters of the algorithm were adjusted in such a way that the inspection conditions defined by the industrial process are fulfilled: 100% detection of all defects, 100% classification of all structural defects as structural ones, and <10% false classified nondefective surfaces, see Section 2. The classification results are depicted in Table 3.

We observed that these classification results are conform with the constrains defined in the industrial requirements. Some image examples with corresponding classification results are shown in Figure 14.

The first group of images (Figures 14(a)–14(d)) shows examples of typical surfaces. Figures 14(a)-14(b) depicts

Table 3: Classification of image set $w_{\text{te}} \in \mathbb{R}^{188}$ recorded under industrial real time conditions using the proposed algorithm. The classification task consists in assigning each image of set w_{te} to one of the three distinct classes Ω_A, $\Omega_{R,S}$, and $\Omega_{R,T}$.

		True state		
		Ω_A	$\Omega_{R,S}$	$\Omega_{R,T}$
Detected state	Ω_A	94	0	0
	$\Omega_{R,S}$	8	51	6
	$\Omega_{R,T}$	0	0	29

True state/detected state

$\Omega_{R,S}/\Omega_{R,S}$ (a) $\Omega_{R,S}/\Omega_{R,S}$ (b) $\Omega_{R,T}/\Omega_{R,T}$ (c) Ω_A/Ω_A (d)

$\Omega_{R,T}/\Omega_{R,S}$ (e) $\Omega_{R,T}/\Omega_{R,T}$ (f) Ω_A/Ω_A (g) $\Omega_A/\Omega_{R,T}$ (h)
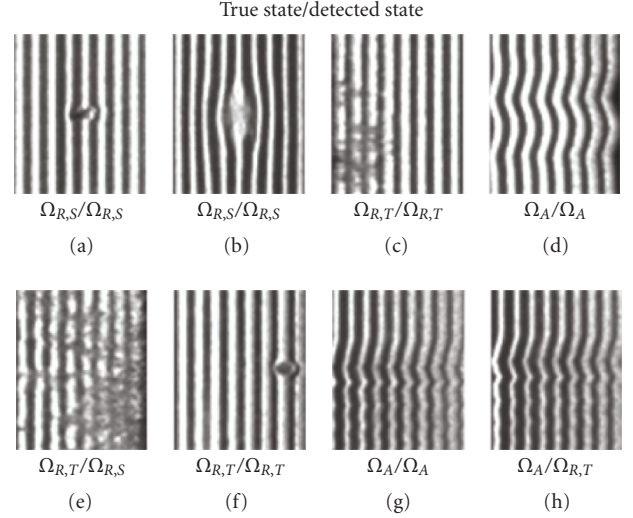
Figure 14: Examples of classified images $\mathbf{f}$ of set w_{te}. Images (a) and (b) show two good classified textural defects. The former has a size of ~0.3 mm and the latter of ~1.5 mm. Images (c) and (d) show two good classified images representing a structural and a recording artefacts. Images (e) and (f) depict a textural defect (classified as structural) and a good classified textural surface. Images (g) and (h) are nearly the same recording artefact, but the former was classified whereas the latter was wrongly classified as a textural surface.

structural defects of different sizes, a textural defect is shown in Figure 14(c) and a recording artefact can be seen in Figure 14(d).

The second image group gives a good impression of the difficulty of the discrimination task. Figure 14(e) expresses a wrongly classified textural defect as a structural one. Using this image and the image shown in Figure 14(f), we observed that the size of bright stripes deviation is approximately the same, namely of half a period $d(P)$. But, the former was classified as textural whereas the latter as structural by the visual inspector. Maybe because the human vision also integrates the size of the defect in his judgement, the real depth of a defect is certainly more difficult to appreciate when the structural disturbances are small and cover a huge surface region.

Our last remark concerns the two last images, Figures 14(g) and 14(h) both depict similar recording artefacts. But if the former was classified as a nondefective surface the latter was falsely classified as textural defect. The reason is of course the bad image quality, both average shape $\hat{S}$ values of 0.56 and 0.53 and average intensity values of 192 and 191

correspond to structural and textural values; see Figure 13. Another important factor explaining the bad discrimination is the "contrast" of the bright lines, which is much less steep than in Figures 14(a) or 14(b) for example.

8. CONCLUSION

In this paper, we presented an original usage of adapted structural illumination. This lighting technique integrates a Lambertian diffuse part for the inspection of specular surfaces *and* a light aperture to project a structured light on the inspected surface. The geometries of both are adapted to the shape of the inspected objects, so that a simple periodical pattern is observed in the images.

We demonstrated that a good enhancement of structural and textural defects (without revealing nondefective surfaces in the same time) is achieved. All the necessary information is contained in one camera image, no stereo vision is needed to discriminate the different nondefective surface types.

We also compared the proposed approach with diffuse and retroreflector lighting techniques. This shows some difficulties in enhancing all structural defects, whereas the second tends to be too sensitive as a noncritical surface structure.

We validated the proposed lighting technique using the images recorded by a daily used industrial application integrating such an adapted structured illumination. These images are classified using a segmentation and classification algorithms. No calibration of the recording setup elements, which are the sensor, the illumination, and the specular surface is needed. We show that a good discrimination of textural, structural, and nondefective surfaces with nonoptimal recording conditions, that is with recording artefacts, is possible.

The next step will be to consider 2.5D rather than 3D technique to measure the depth of the defects with only one camera and one adapted illumination. Based on a simple calibration procedure, we want to propose a new deflectometric approach with an adapted structured illumination.

LIST OF SYMBOLS OF THE MAIN COMPONENTS

(C):	Recording camera sensor
(L):	Light source/illumination
(S):	Whole surface to inspect
(S_{inspect}):	Surface inspected with one camera
(s):	Elementary inspected surface
ρ:	Specular reflectance coefficient, %
α:	Specular reflectance angle, rad
Π_{scan}:	Recording plane of a line-scan camera
$(\text{LP}_{\text{projected}})$:	Projected illumination pattern on (S)
$(\text{LP}_{\text{reflected}})$:	Reflected illumination pattern by (S)
N_r:	Number of projected rays by (L)
$(d_{P,\text{mm}})$:	Illumination pattern period, mm
$(d_{P,\text{px}})$:	Illumination pattern period, pixel
$\mathbf{f}$:	Image pattern
(x_w, y_w, z_w):	World coordinate system
(u, v):	Image coordinate system.

REFERENCES

[1] S. Schuetz, Gewinnung von 3-d-Information durch Strukturierte Beleuchtung, 200.

[2] P. Lang, " *Multisensorielle Pruefung von Freiformflaechen*, Ph.D. thesis," Fraunhofer, Stuttgart, Germany, 1999.

[3] O. Hall-Holt and S. Rusinkiewicz, "Stripe boundary codes for real-time structured-light range scanning of moving objects," in *Proceedings of the 8th International Conference on Computer Vision (ICCV '01)*, vol. 2, pp. 359–366, Vancouver, BC, Canada, July 2001.

[4] T. P. Monks, J. N. Carter, and C. H. Shadle, "Colour encoded structured light for digitisation of real-time 3-d data," in *Proceedings of the IEE 4th International Conference on Image Processing*, pp. 327–330, Maastricht, The Netherlands, April 1992.

[5] H. Ortiz and M. Paterson, "Location and shape measurement using a portable fringe projection system," Experimental Mechanics , vol. 45, no. 3, pp. 197–204, 2005.

[6] S. Winkelbach and F. Wahl, "Shape from single stripe pattern illumination," in *Proceedings of the 24th DAGM Symposium on Pattern Recognition*, vol. 2449 of *Lecture Notes in Computer Science*, pp. 240–247, Zurich, Switzerland, September 2002.

[7] Isra, "A fast paper inspection system," Tech. Rep., Isra Vision System AG, Darmstadt, Germany, 2005.

[8] F. P. León and J. Beyerer, "Active vision and sensor fusion for inspection of metallic surfaces," in *Proceedings of the Intelligent Robots and Computer Vision XVI: Algorithms, Techniques, Active Vision, and Materials Handling*, vol. 3208 of *Proceedings of SPIE*, pp. 394–405, Pittsburg, Pa, USA, September 1997.

[9] CLK: Beetanalyser, Industry product information http://www.clkgmbh.de/geschaeftsfelder-produkte/food-packing/.

[10] R. L. Reynolds, F. Karpaia, D. A. Claarke, and O. L. Hageniers, "Theory and applications of a surface inspection technique using double-pass retroreflection," Optical Engineering , vol. 32, no. 9, pp. 2122–2129, 1993.

[11] H. Marguerre, "Kontrastierverfahren fuer Kruemmungen und Welligkeiten an Oberflaechen zur Qualitaetspruefung," z. b. von Lackoberflaechen. Feinwerktechnik und Messtechnik 9, 1985.

[12] A. Jordan, F. Kahmann, and F. Luecking, "Dual solution for high-end stripe inspection," Material Testing , vol. 26, no. 4, pp. 66–71, 2003.

[13] M. C. Knauer, J. Kaminski, and G. Haeusler, "Phase measuring deflectometry: a new approach to measure specular freefrom surfaces," Optical Metrology in Production Engineering, vol. 5457, pp. 366–376, 2004.

[14] H. Niemann, Pattern Analysis and Understanding , Springer Series in Information Sciences, Springer, Berlin, Germany, 2nd edition, 1990.

[15] S. Kammel and F. P. León, "Head-mounted display for interactive inspection of painted free-form surfaces," in *Proceedings of the International Society for Optical Engineering*, vol. 5079

of *Proceedings of SPIE*, pp. 254–264, Orlando, Fla, USA, April 2003.

[16] S. Kammel and F. P. León, "Deflektometrie zur qualitäts-prüfung spiegelnd reflektierender oberflächen," Technisches Messen , vol. 70, no. 4, pp. 193–198, 2003.

[17] S. Kammel, " *Deflektometrische untersuchung spiegelnd reflek-tierender freiformflchen*, Ph.D. thesis," University of Karlsruhe (TH), Karlsruhe, Germany, 2004.

[18] D. Pérard, " *Automated visual inspection of specular surfaces with structured-lighting reflection techniques, no. 869*, Ph.D. thesis," VDI Verlag, üsseldorf, Germany, 2001.

[19] R. B. Fisher and D. K. Naidu, "A comparison of algorithms for subpixel peak detection," in Advances in Image Processing, Multimedia and Machine Vision , J. Sanz, Ed., pp. 385–404, Springer, Heidelberg, Germany, 1996.

[20] Y. Yang and X. Liu, "A re-examination of text categoriza-tion methods," in *Proceedings of the 22nd Annual International ACM SIGIR Conference on Research and Development in In-formation Retrieval (SIGIR '99)*, pp. 42–49, ACM Press, New York, NY, USA, 1999.